

Zhen Ren¹

Mem. ASME
Mechanical Engineering,
Michigan State University,
East Lansing, MI 48824
e-mail: renzhen@msu.edu and
zhen.ren@delphi.com

Guoming G. Zhu²

Fellow ASME
Department of Mechanical Engineering,
Department of Electrical and
Computer Engineering,
Michigan State University,
1497 Engineering Research Court,
Room E148,
East Lansing, MI 48824
e-mail: zhug@egr.msu.edu

Modeling and Control of an Electric Variable Valve Timing System

This paper presents a model of an electric variable valve timing (EVVT) system and its closed-loop control design with experimental validation. The studied EVVT uses a planetary gear system to control the engine cam timing. The main motivation of utilizing the EVVT system is its fast response time and the accurate timing control capability. This is critical for the combustion mode transition control between the spark ignition (SI) and homogeneous charge compression ignition (HCCI) combustion, where the engine cam timing needs to follow a desired trajectory to accurately control the engine charge and recompression process. A physics-based model was developed to study the characteristics of the EVVT system, and a control oriented EVVT model, with the same structure as the physics-based one, was obtained using closed-loop system identification. The closed-loop control strategies were developed to control the EVVT to follow a desired trajectory. Both simulation and bench test results are included. [DOI: 10.1115/1.4025914]

1 Introduction

Variable valve timing (VVT) systems, used in internal combustion engines, were developed in the nineties [1] and have since been widely used due to the growing fuel economy demands and emission regulations. VVT systems improve fuel economy and reduce emissions at low engine speed, and improve engine power and torque at high engine speed. Conventional electronic-hydraulic VVT [1,2], also called hydraulic VVT, is the most widely used in the automotive engines today. The hydraulic VVT systems require minor changes when applied to traditional non-VVT valve-trains [1], which make design and manufacturing relatively easy. However, due to its mechanism, the hydraulic VVT system also has its limitations [3].

The performance of hydraulic VVT systems is significantly affected by the engine operational conditions such as engine oil temperature and pressure. For instance, at low engine temperature, the hydraulic VVT system cannot be activated and has to remain at its default lock position so that the cold start performance and emissions cannot be improved [3]. This leads to the study of other variable valve-train systems, such as electromagnetic [4], hydraulic [5], electropneumatic [6], and electric motor-driven planetary gear systems [7,8]. Comparing to hydraulic VVT, the electric motor-driven VVT (or electric VVT) is that its performance is less dependent of engine oil temperature and pressure [3]; and it has wider operational range, and hence, it improves engine performance over a wider operational range. Especially, since the EVVT system is actuated by an electric motor, its performance, such as response time, is independent of the engine oil pressure and can be greatly improved by selecting a proper electric motor.

The major advantage of HCCI combustion is realized by eliminating the formation of flames. That results in much lower combustion temperature. As a result, the formation of NO_x (nitrogen oxides) is greatly reduced. The lean burn nature of the HCCI combustion also enables unthrottled operation to improve engine fuel economy. Unfortunately, HCCI combustion is feasible only over a

limited engine operational range due to engine knock at high load and misfire at light load. Achieving HCCI in an automotive internal combustion engine requires it to operate in the SI combustion mode at high load and in the HCCI combustion mode at low and medium load [9,10]. This makes it necessary to have a smooth transition between SI and HCCI combustion modes.

Achieving HCCI combustion and controlling the mode transition between SI and HCCI combustion in a practical engine require a few enabling actuating and sensing technologies. They are used to control the thermodynamic and gas mixture conditions in the combustion chamber at the intake valve closing. The engine actuating subsystems under consideration includes variable valve actuation (cam-based or camless), dual fuel systems (port and direct fuel injection with multiple fuel injections), supercharger and/or turbocharger, exhaust energy recuperation and fast thermal conditioning of the intake charge mixture, spark-assist HCCI combustion, etc. Variable valve actuation can be used to control the effective compression ratio (via the intake valve closing time), the internal residual fraction via the negative valve overlap (also called recompression); see Refs. [11,12], or secondary opening of the exhaust valve (residual re-induction); see Refs. [11,12]. Although hydraulic VVT systems played critical roles in accomplishing smooth mode transitions from SI to HCCI and vice versa, see Refs. [13–15], in addition to providing the basic control of the HCCI combustion (i.e., ignition timing and burn rate or duration), its slow response time limits the performance of mode transition and extends the transition duration. A typical EVVT system is more than five times fast than the traditional VVT one and is capable of accurately tracking the desired cam phase. The EVVT system studied in this paper was used to control the engine valve timings at either SI or HCCI combustion mode, and to track the desired cam phase trajectory during the combustion mode transition for optimized performance.

A feedback controller was introduced in Ref. [8] to control the electric planetary VVT system. The closed-loop EVVT system needs to meet both steady-state regulation and dynamic tracking performance requirements, due to the steady-state and transient requirements of the HCCI combustion. Therefore, a feedback control combined with the feedforward control was developed for the simulation study. The cam phase is the integration of speed difference between the EVVT motor and engine camshaft in an EVVT system. This leads to using the camshaft reference speed as the feedforward control for the EVVT motor. An output covariance constraint (OCC) controller [16–18], an H_2 controller with

¹Present address: Delphi Powertrain Systems, Auburn Hills, MI 48326.

²Corresponding author.

Contributed by the Dynamic Systems Division of ASME for publication in the JOURNAL OF DYNAMIC SYSTEMS, MEASUREMENT, AND CONTROL. Manuscript received September 10, 2012; final manuscript received October 24, 2013; published online December 16, 2013. Assoc. Editor: Xubin Song.

specially selected output weight [18], was used for feedback control to reduce both steady-state and tracking errors. Performance of the OCC controller was compared to well-tuned proportional-derivative (PD) controllers, and the OCC controller with feedforward provides improved cam phase tracking control over the PD control. Different cam phase sample rates were also studied and results show that four samples per engine cycle are sufficient for the OCC feedback control.

The physical-based model and simulation results provide a modeling and control framework for the EVVT bench. The EVVT system with a local speed controller was mounted on an engine head. An electric motor was used to simulate the rotating engine crankshaft. The EVVT pulley was connected to the motor through a timing belt. Because of the complexity of the actual system and unknown motor local speed control parameters, the developed physical-based model was difficult to calibrate. As a result, closed-loop system identification [19] was used to obtain the model calibrations. The q -Markov COVariance Equivalent Realization (q -Markov Cover) system identification method [20–22] using PRBS (pseudorandom binary signal [22]) was used to obtain the closed-loop system models. The EVVT open-loop system model was calculated based upon the identified closed-loop model. The q -Markov Cover theory was originally developed for model reduction. It guarantees that the reduced order system model preserves the first q -Markov parameters of the original system. The realization of all q -Markov Covers using input and output data of a discrete-time system is capable of system identification. Q -Markov Cover for system identification uses pulse, white noise, or PRBS as input excitations. It can be used to obtain the linearized model with matching input/output sequence for nonlinear systems [22]. It was also extended to identify multirate discrete-time systems when input and output sampling rates are different [23]. An OCC controller [18] was designed based upon the identified model.

This paper is organized as following. Section 2 describes the EVVT model and system architecture. Section 3 introduces the feedforward control and the closed-loop OCC control design. Section 4 provides the simulation results. EVVT test bench setup is discussed in Sec. 5. System identification frameworks are discussed in Sec. 6; and the experimental results are shown in Sec. 7, along with the study of performance impact of the engine oil viscosity. Conclusions are drawn in Sec. 8.

2 EVVT Modeling

2.1 Planetary EVVT Components. The planetary gear EVVT system studied in this paper consists of four major components (see Fig. 1). Ring gear, serves as VVT pulley, is driven directly by a crankshaft through a timing belt at half crankshaft speed. Planet gear carrier is driven by an electric motor. Planet

gears engage both ring and sun gears. Sun gear is connected to the camshaft. The sun and planet gears are passive components that obtain kinetic energy from carrier and ring gears. Comparing to other components, the inertia of engine fly wheel and crankshaft is fairly large. As a result, dynamics of the ring gear is ignored in the model. All other components have known mechanical properties and their dynamics are considered in the modeling.

2.2 Planetary Gear System Kinematics. In a planetary gear system [24] shown in Fig. 1, angular velocities of components are determined by

$$\frac{\omega_s(t) - \omega_c(t)}{\omega_r(t) - \omega_c(t)} = -\frac{n_r}{n_s} \quad (1)$$

where ω_s , ω_c , and ω_r are angular velocities of the sun, carrier, and ring gears, respectively. n_r and n_s are the teeth numbers of ring and sun gears. Laplace transformation [25] of Eq. (1) can be expressed as

$$\Omega_s(s) = -\frac{n_r}{n_s}\Omega_r(s) + \frac{n_r}{n_s}\Omega_c(s) + \Omega_c(s) \quad (2)$$

The cam phase angle ϕ is the integration of the double difference between camshaft and crankshaft speeds. That is

$$\phi = 2 \int_0^t [\omega_s(\tau) - \omega_r(\tau)] d\tau \quad (3)$$

and its corresponding Laplace transformation is

$$\Phi(s) = \frac{2}{s} [\Omega_s(s) - \Omega_r(s)] \quad (4)$$

Substituting Eq. (2) into Eq. (4) yields

$$\Phi = \frac{2}{s} \left(\frac{n_s + n_r}{n_s} \right) (\Omega_c - \Omega_r) \quad (5)$$

Equation (5) shows that the cam phase is an integral function of speed difference between carrier and ring gears. By controlling the EVVT motor speed with respect to the engine crankshaft speed, cam phase can be adjusted. When the carrier speed is equal to the ring speed, cam phase is held; when the carrier speed is greater than the ring speed, cam phase is advancing; and when the carrier speed is slower than the ring speed, cam phase is retarding. Notice that Eq. (5) contains an integrator, and target cam phase reference cannot be used as feedforward control directly.

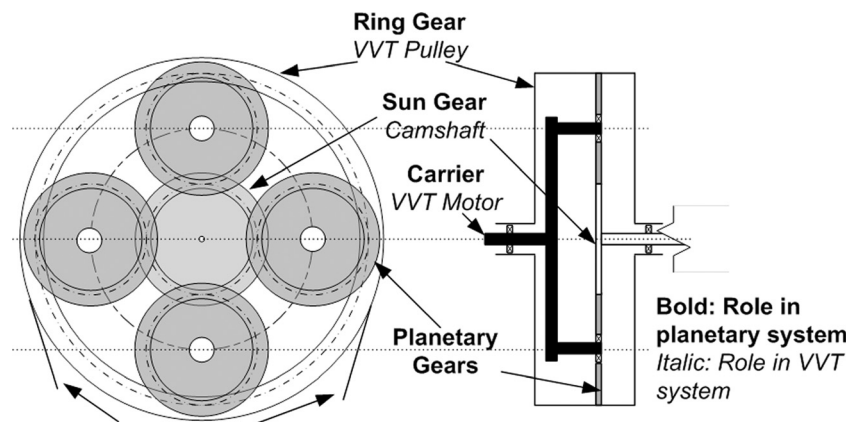


Fig. 1 Electric planetary gear VVT system

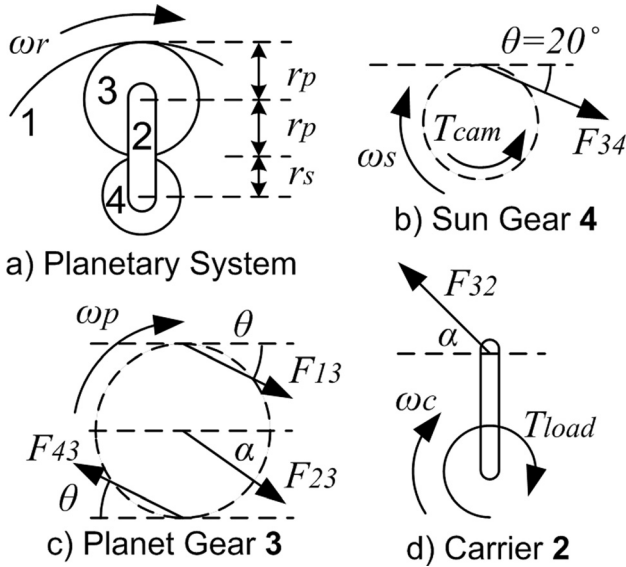


Fig. 2 Free body diagrams of planetary gear components

2.3 Planetary Gear System Dynamics. Planetary gear system dynamics with an electric motor are modeled in this section. For simplicity, the gear system friction is ignored in this modeling study. Figure 2 shows free body diagrams of planetary gear components.

Without loss of generality comparing with the system in Fig. 1, the system is treated as having only one planet gear (Fig. 2(a)). Assuming that all the gears are properly engaged, the following equation is derived:

$$\frac{n_s}{r_s} = \frac{n_p}{r_p} = \frac{n_r}{r_r}, \quad r_r = 2r_p + r_s \quad (6)$$

where n_p is planet gear number of teeth. r_s , r_p , and r_r are pitch circle radius of sun, planet, and ring gears, respectively. In this study, the gears use a standard pressure angle θ of 20 deg. Since the ring has a very large inertia comparing to other components, angular velocity of the ring ω_r is assumed to be constant during the phase shifting. From Eq. (2)

$$\dot{\omega}_s = \frac{n_r + n_s}{n_s} \dot{\omega}_c \quad (7)$$

There are two torques applied to the sun gear (Fig. 2(b)). They are camshaft load T_{cam} and torque from tooth force F_{34} .

$$F_{34} \cdot r_s \cdot \cos \theta - T_{cam} = J_s \dot{\omega}_s \quad (8)$$

where J_s is sun gear's moment of inertia with respect to its center of gravity.

Two tooth forces (F_{43} and F_{13}) and one bearing force from carrier F_{23} are applied to planet gear (see Fig. 2(c)) that rotates around the bearing on the carrier at ω_p

$$\frac{\omega_p(t) - \omega_c(t)}{\omega_s(t) - \omega_c(t)} = -\frac{n_s}{n_p} \quad (9)$$

and from torque balance with respect to bearing point

$$(F_{43} + F_{13}) \cdot r_p \cdot \cos \theta = J_p \dot{\omega}_p \quad (10)$$

where J_p is planet gear moment of inertia with respect to its center of gravity. The planet gear also rotates about the center of sun gear. Therefore

$$[F_{13}(2r_r) - F_{43}r_s] \cos \theta + F_{23}(r_p + r_s) \cos \alpha = J_{ps} \dot{\omega}_c \quad (11)$$

where the direction and magnitude of bearing force F_{23} are unknown. The planet gear moment of inertia with respect to the center of sun gear J_{ps} can be calculated by

$$J_{ps} = J_p[1 + m_p(r_s + r_p)^2] \quad (12)$$

Since the carrier is driven directly by the motor shaft, the carrier inertia is also considered as part of motor shaft inertia, and modeled in Sec. 2.4. Torque balance of carrier is

$$F_{32} \cos \alpha (r_p + r_s) = T_{load} \quad (13)$$

where T_{load} is the mechanical load to the motor shaft and F_{32} is the bearing force from planet gear.

Equations (6)–(13) can be simplified as follows:

$$T_{load} = J_{gears} \dot{\omega}_c + kT_{cam} \quad (14)$$

where constant J_{gears} is an equivalent inertia of the planetary gear system, and k is a factor of gear ratio.

2.4 EVVT Motor Dynamics An electric motor is used to drive carrier in the planetary system. A local closed-loop speed governor is used to control both the motor speed and direction. The input to the local motor controller is the reference speed and direction. The motor and its controller are treated as an actuator in this study (Fig. 3). It is modeled with two inputs of motor velocity command and cam load, and one output of motor shaft speed.

The mechanical load of the motor can be modeled [25] as

$$J_c \dot{\omega}_c = \tau - B\omega_c - T_{load} \quad (15)$$

where J_c is the moment of inertia of motor shaft and carrier, B is the friction coefficient, and τ is the motor torque. Substituting Eq. (14) into Eq. (15) leads to

$$(J_c + J_{gears}) \dot{\omega}_c + B\omega_c = \tau - kT_{cam} \quad (16)$$

and the associated transfer function can be written as

$$\Omega_c(s) = \frac{1}{(J_c + J_{gears})s + B} [T(s) - kT_{cam}(s)] \quad (17)$$

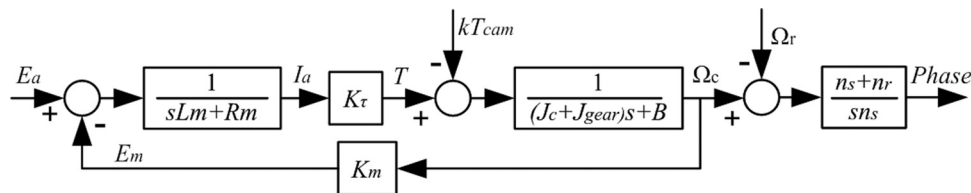


Fig. 3 Block diagram of an electric motor with the planetary gear system

Modeling procedure of the electrical portion can be found in Ref. [25]. Let $J = J_c + J_{\text{gears}}$, the electric motor with planetary gear load (Fig. 3) can then be represented by

$$\Omega_c(s) = G_e(s)E_a(s) + G_m(s)T_{\text{cam}}(s) \quad (18)$$

where the voltage input transfer function is

$$G_e = \frac{K_\tau}{(L_m s + R_m)(Js + B) + K_\tau K_m} \cong \frac{K_\tau}{R_m(Js + B) + K_\tau K_m} \quad (19)$$

and the mechanical input transfer function is

$$G_m = \frac{-(L_m s + R_m)}{(L_m s + R_m)(Js + B) + K_\tau K_m} \cong \frac{-R_m k}{R_m(Js + B) + K_\tau K_m} \quad (20)$$

and K_τ , K_m , L_m , and R_m are the motor parameters representing motor torque constant, back electric magnetic field constant, armature inertia, and resistance, respectively.

Note that the model described by Eqs. (18)–(20) were used to determine the order of the identified system model described in Sec. 6 and used for simulation validation and evaluation of the closed-loop system performance.

3 Feedforward and Closed-Loop Control Design

3.1 OCC. Consider the following state-space linear time-invariant system:

$$\begin{aligned} \mathbf{x}_p(k+1) &= \mathbf{A}_p \mathbf{x}_p(k) + \mathbf{B}_p \mathbf{u}(k) + \mathbf{D}_p \mathbf{w}_p(k) \\ \mathbf{y}_p(k) &= \mathbf{C}_p \mathbf{x}_p(k) \\ \mathbf{z}(k) &= \mathbf{M}_p \mathbf{x}_p(k) + \mathbf{v}(k) \end{aligned} \quad (21)$$

where \mathbf{x}_p is the state; \mathbf{u} is the control input; \mathbf{w}_p represents process noise; and \mathbf{v} is the measurement noise. The vector \mathbf{y}_p contains all variables whose dynamic responses are of interest. Vector \mathbf{z} is the noisy measurements. Suppose that a strictly proper output feedback stabilizing control law, expressed in state-space form below, is employed for plant (21).

$$\begin{aligned} \mathbf{x}_c(k+1) &= \mathbf{A}_c \mathbf{x}_c(k) + \mathbf{Fz}(k) \\ \mathbf{u}(k) &= \mathbf{Gx}_c(k) \end{aligned} \quad (22)$$

where \mathbf{x}_c is the controller state; \mathbf{u} is the control output; and \mathbf{z} is the noisy measurement input. Note that matrices \mathbf{F} , \mathbf{A}_c , and \mathbf{G} are control design parameters. Then, the resulting closed-loop system is

$$\begin{aligned} \mathbf{x}(k+1) &= \mathbf{Ax}(k) + \mathbf{Dw}(k) \\ \mathbf{y}(k) &= \begin{bmatrix} \mathbf{y}_p(k) \\ \mathbf{u}(k) \end{bmatrix} = \begin{bmatrix} \mathbf{C}_y \\ \mathbf{C}_u \end{bmatrix} \mathbf{x}(k) = \mathbf{Cx}(k) \end{aligned} \quad (23)$$

where $\mathbf{x} = [\mathbf{x}_p^T \ \mathbf{x}_c^T]^T$ and $\mathbf{w} = [\mathbf{w}_p^T \ \mathbf{v}^T]^T$. Formulas for the closed-loop system matrices \mathbf{A} , \mathbf{C} , and \mathbf{D} can be obtained based upon Eqs. (21) and (22).

Consider the closed-loop system (23). Let \mathbf{W}_p and \mathbf{V} denote positive definite symmetric matrices with dimensions compatible to the process noise \mathbf{w}_p and measurement vector \mathbf{z} , respectively. Define $\mathbf{W} = \text{block diag}[\mathbf{W}_p \ \mathbf{V}]$ and let \mathbf{X} denote the closed-loop controllability Gramian from the input $\mathbf{W}^{-1/2}\mathbf{w}$. Since \mathbf{A} is stable, \mathbf{X} satisfies

$$\mathbf{X} = \mathbf{AXA}^T + \mathbf{DWD}^T \quad (24)$$

The goal is to find controllers of form (12) that minimize the (weighted) control energy $\text{trace}(\mathbf{RC}_u \mathbf{X} \mathbf{C}_u^T)$ with $\mathbf{R} > 0$ subject to the following constraint:

$$\mathbf{Y} = \mathbf{CXCT}^T \leq \bar{\mathbf{Y}} \quad (25)$$

where $\bar{\mathbf{Y}} > 0$ is given and \mathbf{X} solves (24). This problem, called the OCC problem [18], is defined as finding a full-order dynamic output feedback controller (22) for system (21) that minimizes the following cost

$$J_{\text{occ}} = \text{trace}(\mathbf{RC}_u \mathbf{X} \mathbf{C}_u^T), \quad \mathbf{R} > 0 \quad (26)$$

subject to constraints (24) and (25).

The OCC problem has several interesting interpretations. For instance, assume first that \mathbf{w}_p and \mathbf{v} are uncorrelated zero-mean white noises with intensity matrices $\mathbf{W}_p > 0$ and $\mathbf{V} > 0$. Let E be an expectation operator, and

$$\begin{aligned} E[\mathbf{w}_p(k)] &= 0; & E[\mathbf{w}_p(k)\mathbf{w}_p^T(k-n)] &= \mathbf{W}_p \delta(n) \\ E[\mathbf{v}(k)] &= 0; & E[\mathbf{v}(k)\mathbf{v}^T(k-n)] &= \mathbf{V} \delta(n) \end{aligned} \quad (27)$$

Define $E_\infty[\cdot] := \lim_{k \rightarrow \infty} E[\cdot]$, it is easy to see that OCC is the problem of minimizing $E_\infty \mathbf{u}^T \mathbf{R} \mathbf{u}$ subject to the OCC constraint $\mathbf{Y} := E_\infty \mathbf{y}(k)\mathbf{y}^T(k) \leq \bar{\mathbf{Y}}$. It is well known that this constraint may be interpreted as constraint on the variance of the performance variables or lower bounds on the residence time (in a given ball around the origin of the output space) of the performance variables; see Ref. [26] for details.

The OCC problem can also be interpreted from a deterministic point of view. To see this, define the ℓ_∞ and ℓ_2 norms as follows:

$$\begin{aligned} \|\mathbf{y}\|_\infty^2 &:= \sup_{k \geq 0} \mathbf{y}^T(k)\mathbf{y}(k) \\ \|\mathbf{w}\|_2^2 &:= \sum_{k=0}^{\infty} \mathbf{w}^T(k)\mathbf{w}(k) \end{aligned}$$

and define the (weighted) ℓ_2 disturbance set

$$\mathcal{W} := \left\{ \mathbf{w} : \mathbf{R} \rightarrow \mathbf{R}^{n_w} \text{ and } \|\mathbf{W}^{-1/2}\mathbf{w}\|_2^2 \leq 1 \right\} \quad (29)$$

where $\mathbf{W} > 0$ is a real symmetric matrix. Then, for any $\mathbf{w} \in \mathcal{W}$, the following is true (see Refs. [27,28] for details)

$$\|\mathbf{y}\|_\infty^2 \leq \bar{\sigma}[\mathbf{Y}], \text{ and } \|\mathbf{u}_i\|_\infty^2 \leq [\mathbf{C}_u \mathbf{X} \mathbf{C}_u^T]_{ii}, \quad i = 1, 2, \dots, n_u \quad (30)$$

where n_u is the dimension of \mathbf{u} ; $\bar{\sigma}[\cdot]$ denotes the maximum singular value; and $[\cdot]_{ii}$ is the diagonal entry. Moreover, Refs. [27,28] show that the bounds in Eq. (30) are the least upper bounds for any signal $\mathbf{w} \in \mathcal{W}$.

Thus, using $\bar{\mathbf{Y}} = I\epsilon^2$ in Eq. (25) and $\mathbf{R} = \text{diag}[r_1, r_2, \dots, r_{n_u}]$ in Eq. (26), the OCC is the problem of minimizing the weighted sum of worst-case peak values on the control signals (related to actuator sizing) given by

$$J_{\text{occ}} = \sum_{i=1}^{n_u} r_i \left\{ \sup_{\mathbf{w} \in \mathcal{W}} \|\mathbf{u}_i\|_\infty^2 \right\} \quad (31)$$

subject to the constraint on the worst-case peak value of the performance variables of the form

$$\sup_{\mathbf{w} \in \mathcal{W}} \|\mathbf{y}\|_\infty^2 \leq \epsilon^2 \quad (32)$$

This interpretation is important in applications where hard constraints on responses or actuator signals cannot be ignored such as space telescope pointing error and machine tool control problems. Detailed proof can be found in Ref. [16]. The controller matrices \mathbf{A}_c , \mathbf{F} , and \mathbf{G} can be calculated using an iterative algorithm introduced in Refs. [16,18].

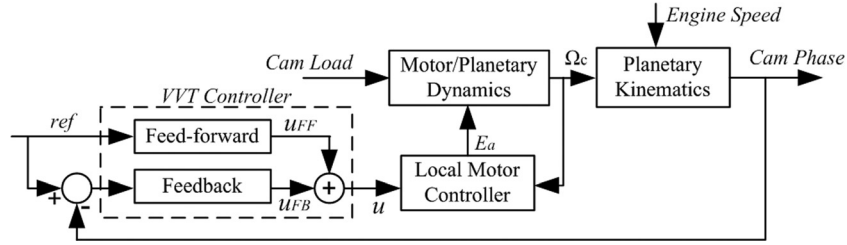


Fig. 4 EVVT control system architecture

3.2 Control Design Parameters. The EVVT system model includes the VVT controller, the local motor controller, motor/planetary dynamics, and planetary kinematics. Figure 4 shows an overview of the control system architecture. The system parameters are listed as following and the controllers were designed based on these parameters.

The voltage input transfer function is

$$G_e = \frac{45}{0.2s + 1} \quad (33)$$

the mechanical input transfer function is

$$G_m = \frac{-5}{0.2s + 1} \quad (34)$$

and the motor has a local proportional integral derivative (PID) controller defined by

$$K_{\text{motor}} = 1 + \frac{0.1}{s} + 0.05 \left(\frac{s}{0.01s + 1} \right) \quad (35)$$

Teeth numbers of the gear-train are listed in Table 1. Substituting these values into Eq. (5) results the planetary kinematics

$$\Phi = \frac{6}{s} (\Omega_c - \Omega_r) \quad (36)$$

Figure 5 describes the cam torque load of each cylinder over an engine cycle. It consists of three portions: constant friction load, sinusoidal load representing cam profile, and steps represent the valve spring preload. In the study, a four cylinder engine is simulated. The total load is a combination of four single cylinder loads with 180deg phase shift for each cylinder, assuming the cam drives both intake and exhaust valves.

3.3 Feedforward Control. A feedforward controller was employed to improve the system response. The reference cam phase was not used directly as feedforward control due to the physical characteristics of the EVVT system stated in Sec. 3.2; instead, the derivative of the cam phase reference signal was used due to the planetary kinematics shown in Eq. (36). The feedforward gain was determined by the ratio between desired cam phase slope and the motor speed. Using Eq. (36), feedforward gain K_{FF} can be determined as

$$u_{FF} = K_{FF} \dot{\theta}_{ref} + \omega_r = \frac{1}{6} \dot{\theta}_{ref} + \omega_r \quad (37)$$

where u_{FF} is the feedforward control effort. $\dot{\theta}_{ref}$ is the filtered derivative of the reference signal θ_{ref}

Table 1 Planetary system parameters

Component	Sun	Ring	Planet
Number of teeth	30	60	15

$$\dot{\theta}_{ref} = \frac{s}{0.05s + 1} \theta_{ref} \quad (38)$$

3.4 Baseline Control. Since the electrical cam phase actuator plant contains an integrator, PD controllers were used as our baseline ones. Two baseline feedback controllers were tuned for performance comparison, where PD_{WF} was tuned without feedforward and PD_{WOF} was tuned with feedforward, and they are

$$\begin{aligned} PD_{WF}(s) &= 7 + 0.03s \\ PD_{WOF}(s) &= 1 + 0.005s \end{aligned} \quad (39)$$

3.5 OCC Feedback Control Design. The OCC control design considers the mechanical cam load as a disturbance, the EVVT controller input as a plant input, and the cam phase as an output, the electrical portion system matrices of the EVVT system (Fig. 4) can then be written as

$$\begin{aligned} \mathbf{A} &= \begin{bmatrix} -1455 & -23023 & -2250 & 0 \\ 1 & 0 & 0 & 0 \\ 0 & 1 & 0 & 0 \\ 0 & 0 & 1 & 0 \end{bmatrix}, \quad \mathbf{B} = \begin{bmatrix} 1 \\ 0 \\ 0 \\ 0 \end{bmatrix} \\ \mathbf{C} &= [0 \quad 8100 \quad 135130 \quad 13500], \quad \mathbf{D} \cong 0 \end{aligned} \quad (40)$$

The control design parameters were chosen as

$$\mathbf{W}_p = 2, \quad \mathbf{V} = 0.01, \quad \mathbf{R} = 1 \quad (41)$$

Using the control design algorithm introduced in Ref. [18], the resulting OCC controller is

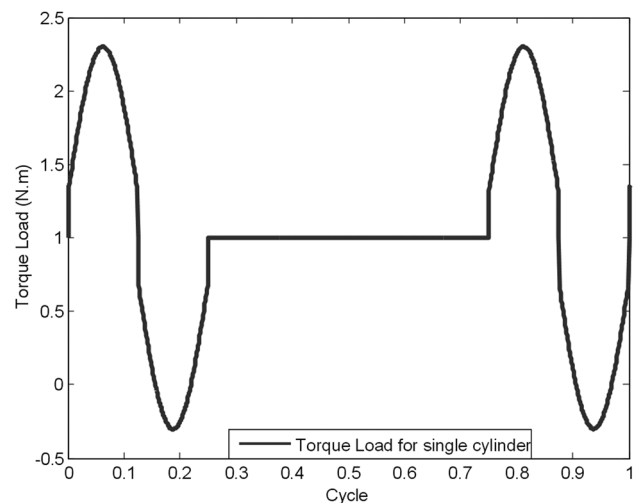


Fig. 5 Torque load for single cylinder

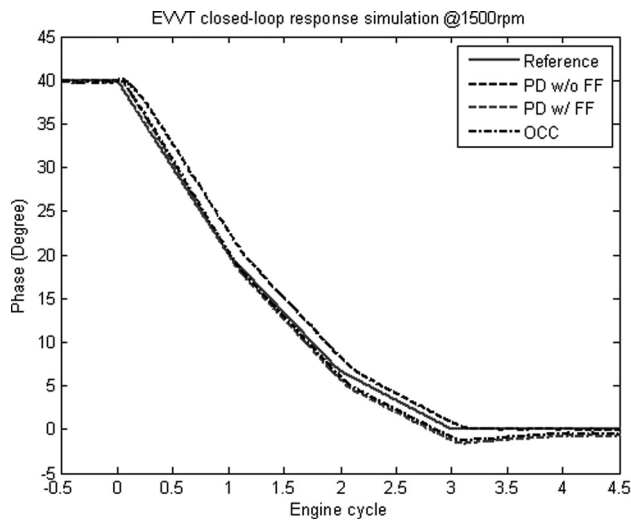


Fig. 6 Simulated cam phase responses at 1500 rpm

$$K = \frac{113.6s^3 + 1.65 \times 10^5 s^2 + 2.6 \times 10^6 s + 2.6 \times 10^5}{s^4 + 1541s^3 + 1.5 \times 10^5 s^2 + 2.12 \times 10^6 s + 2.11 \times 10^5} \quad (42)$$

The system transfer function (42) and its state-space realization (40) provide a system model for control design and simulation study conducted in Sec. 4; and it also provide the system order selection information for system identification conducted in Sec. 6.

4 Simulation Study

The EVVT reference signal was selected as a forty crank degree phase retard that completes in three engine cycles to simulate the EVVT operation under SI and HCCI combustion transition. The transition reference signal is divided into three stages with a constant slope within one engine cycle for simplicity. The retard phase is 50% (20 deg) for the first engine cycle, 33.3% (40/3 deg) for the second cycle, and 16.7% (20/3 deg) for the third. The phase control signal was sampled every 5 ms and the feedback signal is updated four times per engine cycle. For instance, at 1500 rpm the cam phase is sampled every 20 ms. The closed-loop system performance at two engine speeds, 1500 rpm and 2000 rpm, was studied.

Figure 6 compares the cam phase responses among three controllers, OCC, PD_{WF}, and PD_{WOF} at 1500 rpm. It shows that the initial response of the PD controller with feedforward (PD_{WF}) is much faster than the PD controller without feedforward (PD_{WOF}). However, due to the relatively low gain of the PD controller with feedforward, after the second cycle, it has a larger overshoot with longer settling time than the PD controller without feedforward. However, the OCC controller demonstrates fast response time with low overshoot. Table 2 shows cam phase angles at the end of each engine cycle after the SI and HCCI transition starts. The OCC controller with feedforward has the lowest overall tracking errors. Figure 7 provides the same time responses as Fig. 6 at 2000 rpm. It is noticed that the performance is quite different at engine speeds of 1500 and 2000 rpm (see Figs. 6 and 7). Table 2 compares the cam phase error at the end of each engine cycle numerically and shows that the tracking error increases at 2000 rpm. This could be due to the increased rate change of the reference cam phase signal in time domain as the engine speed increases from 1500 to 2000 rpm since the engine cycle period reduced from 80 ms at 1500 rpm to 60 ms at 2000 rpm.

The tracking errors with increased feedback sampling rates were also studied and the results are shown in Table 3. The simulation data show that the tracking error reduces when the number of samples increased from four samples per engine cycle to eight.

Table 2 Output comparison at end of each cycle

Engine speed	Cycle number	Error (deg)		
		PD	PD w/ ff	OCC w/ ff
1500 rpm	1	+2.6	+0.1	+0.3
	2	+1.8	-1.0	-0.6
	3	+0.8	-1.3	-0.8
	4	+0.0	-0.8	-0.5
2000 rpm	1	+2.5	+0.1	+0.4
	2	+1.7	-1.2	-0.7
	3	+1.0	-1.1	-0.6
	4	-0.2	-1.3	-0.9

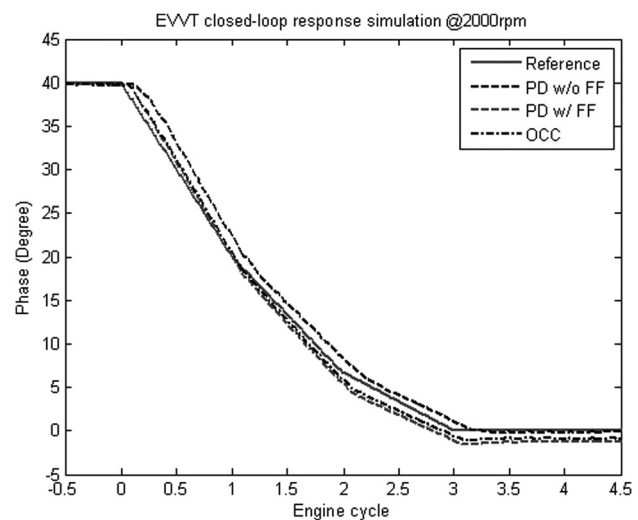


Fig. 7 Cam phase output comparison at 2000 rpm

Table 3 Output comparison at 2000 rpm with different sample rate

Sample rate	Cycle number	Error (deg)		
		PD	PD w/ ff	OCC w/ ff
8/ cycle	1	+2.2	+0.4	+0.7
	2	+1.5	-0.5	+0.0
	3	+0.8	-1.0	-0.5
	4	+0.2	-0.6	-0.4
16/ cycle	1	+2.2	+0.6	+0.9
	2	+1.5	-0.2	+0.4
	3	+0.7	-0.6	-0.2
	4	+0.0	-0.5	-0.1

However, further increment of number of samples does not reduce the tracking error significantly. Especially, with the OCC design, the tracking error is fairly small with four samples per cycle. Therefore, considering the limited tracking error reduction and increased computational requirement with high sample rate, it is determined that using four samples per engine cycle is proper for this application.

As a summary, simulation results show that the OCC controller has a lower overshoot than a well-tuned proportional controller, while with comparable response time, and four samples per engine cycle for the cam position is suitable for the EVVT control application.

5 The EVVT Test Bench Setup

A test bench was constructed for system identification and control validation of the studied EVVT actuator system. The test

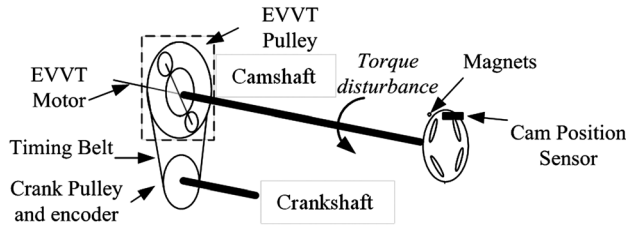


Fig. 8 EVVT system test bench diagram

setup was very similar to the hydraulic VVT system bench [19], except the hydraulic VVT was replaced by an EVVT system. The EVVT system has a phasing range of 45 deg and is controlled by an AC motor with its own PID speed governor. An Opal-RT (Hardware-in-the-loop test equipment manufacture, located in Montréal, Québec, Canada) real-time prototype controller controls the cam phase by adjusting the reference speed pulse-width modulation (PWM) signal sent to the motor speed governor. The PWM signal frequency is directly proportional to the command speed and the local motor controller has its own cut-off frequencies at both high and low motor speeds.

A Ford 5.4L V8 engine head was used for the test bench. An electric motor was used to simulate the motion of the engine crank shaft. An encoder was installed on the motor shaft that generates crank angle and gate (360 deg per pulse) signals. A hall-effect cam position sensor was installed with a four-slot cam disc, which generates four pulses per engine cycle. Therefore, the cam position is updated four times every engine cycle. Figure 8 shows the diagram of the EVVT test bench with key system components and Fig. 9 is a picture of the associated test bench. The cam position sensing system has a theoretical resolution of 1/64 crank degree. An electric oil pump was used to supply oil for the valve-train system and the EVVT planetary gear system, and the EVVT bench was running at room temperature (25 °C). This setup enables the system identification and control experimental work.

6 System Identification Framework

Consider a general form of linear time-invariant closed-loop system shown in Fig. 10, where r is the reference signal; n is the measurement noise; u and y are system input and output, respectively. As discussed in Sec. 1, there are many approaches for the closed-loop system identification, which can be categorized as direct, indirect, and joint input-output approaches. In this paper, the controller knowledge is used to calculate the open-loop plant model from identified closed-loop system model, which is called

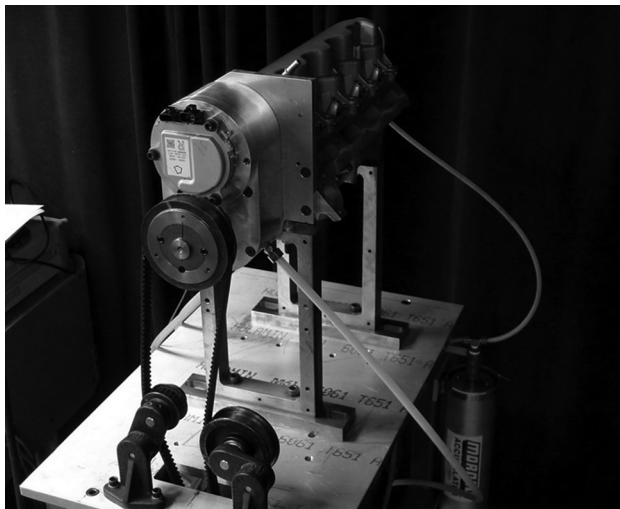


Fig. 9 EVVT test bench

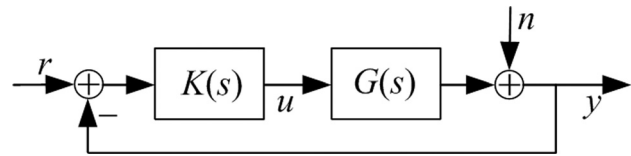


Fig. 10 Closed-loop identification framework

indirect approach. To ensure the accuracy of the identified plant, the closed-loop controller in this paper was selected to be proportional [29,30].

The input and output relationship of the generalized closed-loop system, shown in Fig. 10, can be expressed below:

$$y = \mathbf{H} \cdot \mathbf{r} = \mathbf{GK}(\mathbf{I} + \mathbf{GK})^{-1} \mathbf{r} \quad (43)$$

Let $\hat{\mathbf{H}}$ be identified closed-loop transfer functions from r to y . The open-loop system model \mathbf{G}_{ID} can be calculated using identified $\hat{\mathbf{H}}$, assuming that $(\mathbf{I} - \hat{\mathbf{H}})$ is invertible. The controller transfer function is used to solve for the open-loop system models. Then, the following can be derived:

$$\mathbf{G}_{ID} = \hat{\mathbf{H}}(\mathbf{I} - \hat{\mathbf{H}})^{-1} \mathbf{K}^{-1} \quad (44)$$

PRBS signal is used as an input signal for identifying the closed-loop system model. The most commonly used PRBSs are based on maximum length sequences (called m -sequences) [31] for which the length of the PRBS is $m = 2^n - 1$, where n is an integer (order of PRBS). Let z^{-1} represent a delay operator, and define $\hat{p}(z^{-1})$ and $p(z^{-1})$ to be polynomials

$$p(z^{-1}) = a_n z^{-n+1} \oplus \dots \oplus a_2 z^{-1} \oplus a_1 = \hat{p}(z^{-1}) z^{-1} \oplus 1 \quad (45)$$

where a_i is either 1 or 0, and \oplus obeys binary addition, i.e.,

$$1 \oplus 1 = 0 = 0 \oplus 0 \text{ and } 0 \oplus 1 = 1 = 1 \oplus 0 \quad (46)$$

and the nonzero coefficients a_i of the polynomial are defined in the following (Table 4) and also in Ref. [31].

Then, the PRBS can be generated by the following formula

$$\hat{u}(k+1) = \hat{p}(z^{-1})\hat{u}(k), \quad k = 0, 1, 2, \dots \quad (47)$$

where $\hat{u}(0) = 1$ and $\hat{u}(-1) = \hat{u}(-2) = \dots = \hat{u}(-n) = 0$. Defined the following sequence

$$s(k) = \begin{cases} a; & \text{If } k \text{ is even;} \\ -a; & \text{If } k \text{ is odd.} \end{cases} \quad (48)$$

Then, the signal

$$u(k) = s(k) \otimes [-a + 2a\hat{u}(k)] \quad (49)$$

is called the *inverse* PRBS, where \otimes obeys

Table 4 Nonzero coefficients of PRBS polynomial

Polynomial order (n)	Period of sequence (m)	Nonzero coefficient
6	63	a_5, a_6
7	127	a_4, a_7
8	255	a_2, a_3, a_4, a_8
9	511	a_5, a_9
10	1023	a_7, a_{10}
11	2047	a_9, a_{11}

Table 5 Closed-loop identification parameters for the EVVT bench

Engine speed (rpm)	1000	1500
Input sample rate (ms)	5	5
Output sample rate (ms)	30	20
Output/input sample ratio	0.167	0.25
PRBS order	13	13
Signal length (s)	81.88	81.88
Markov parameter, #	100	100
ID open-loop model order	4	4

$$a \otimes a = -a = -a \otimes -a \ \& \ a \otimes -a = -a \otimes a \quad (50)$$

It is clear after some analysis that u has a period $2m$ and $u(k) = -u(k+m)$. The mean of the inverse PRBS is

$$m_u = E_{2m}u(k) \equiv \frac{1}{2m} \sum_{k=0}^{2m-1} u(k) = 0 \quad (51)$$

and the autocorrelation ($R_{uu}(\tau) = E_{2m}u(k+\tau)u(k)$) of u is

$$R_{uu}(\tau) \equiv \frac{1}{2m} \sum_{k=0}^{2m-1} u(k+\tau)u(k) = \begin{cases} a^2, & \tau = 0; \\ -a^2, & \tau = m; \\ -a^2/m, & \tau \text{ even}; \\ a^2/m, & \tau \text{ odd}. \end{cases} \quad (52)$$

Note that the first and second order information of the inverse PRBS signal is very close to these of white noise for a large enough m . The inverse PRBS is used in the q -Markov Cover identification. For convenience, in the rest of this paper, the term ‘‘PRBS’’ is used to represent the inverse PRBS.

Consider an unknown (presumed nonlinear) system

$$\begin{aligned} \mathbf{x}(k+1) &= f(\mathbf{x}(k), \mathbf{w}(k)) \\ \mathbf{y}(k) &= g(\mathbf{x}(k), \mathbf{w}(k)) \end{aligned} \quad (53)$$

subjected to an input sequence $\{w(0), w(1), w(2), \dots\}$ generating the output sequence $\{y(0), y(1), y(2), \dots\}$. The unknown system is q -identifiable, if there exists a linear model of the form:

$$\begin{aligned} \mathbf{x}(k+1) &= (k) + \mathbf{D}\mathbf{w}(k) \\ \mathbf{y}(k) &= \mathbf{C}\mathbf{x}(k) + \mathbf{H}\mathbf{w}(k) \end{aligned} \quad (54)$$

that can reproduced the same output sequence $\{y(0), y(1), y(2), \dots, y(q-1)\}$, subject to the same input sequence $\{w(0), w(1), w(2), \dots, w(q-1)\}$. In case that the system is not

q -identifiable, it is possible for q -Markov Cover to construct the least squares fit using linear model for the input–output sequence (see Refs. [32,33]). The above q -Markov Cover system identification framework was used in Sec. 7 to obtain the linearized EVVT model for control design.

7 EVVT Control System Bench Tests

This section discusses the bench system identification and control design based upon the identified EVVT model. The closed-loop control is presented at the end of the section.

7.1 Closed-Loop Identification of EVVT System. The engine feedforward speed (half engine speed) was used during the system identification. The main reason is that the EVVT model uses the speed difference between the motor and half engine speed as the input; see Eq. (5). Since the engine speed changes much slower than the EVVT phasing speed, it is considered as a constant during the cam phasing. The resulting identified model has the following form:

$$\Phi = G_{\text{evvt}}(s)(u - \frac{1}{2}\omega_{\text{eng}}) \quad (55)$$

where Φ is the cam phase; $G_{\text{evvt}}(s)$ is the identified EVVT model; u is the speed command from the controller; and the constant $\frac{1}{2}\omega_{\text{eng}}$ is half engine speed. The PRBS was used as the reference signal for the closed-loop identification and its amplitude was selected to be 10 deg centered at 20 deg advance from the most retarded position. A proportional controller with a gain of 0.07 was used for the system identification.

The EVVT system was identified at 1000 and 1500 rpm due to the speed limitation on the test bench. Parameters used in the identification are listed in Table 5. The order of the identified EVVT model was chosen to be four that is the same as the physical model (40). A nominal system model was obtained as

$$G_{\text{evvt}}(s) = \frac{-9.7s^3 + 139s^2 + 5760s + 5785}{s^4 + 12.2s^3 + 159s^2 - 62s + 11} \left(\frac{\text{deg}}{1000 \text{ rpm}} \right) \quad (56)$$

7.2 Control Design for EVVT System Test Bench. An OCC controller was designed for the EVVT bench system. The system plant matrices of the nominal model were obtained from Eq. (56)

$$\begin{aligned} \mathbf{A}_p = \mathbf{A} &= \begin{bmatrix} -12.2 & -159 & 62 & -11 \\ 1 & 0 & 0 & 0 \\ 0 & 1 & 0 & 0 \\ 0 & 0 & 1 & 0 \end{bmatrix}, \quad \mathbf{B}_p = \mathbf{B} = \begin{bmatrix} 1 \\ 0 \\ 0 \\ 0 \end{bmatrix} \\ \mathbf{C}_p = \mathbf{M}_p = \mathbf{C} &= [-9.6 \quad 139.9 \quad 5756 \quad 5783], \quad \mathbf{D}_p \cong \mathbf{0} \end{aligned} \quad (57)$$

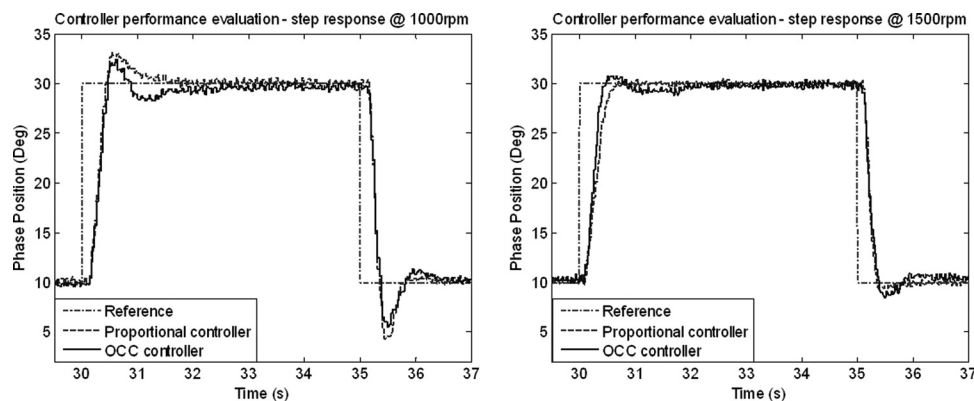


Fig. 11 EVVT bench step response comparison

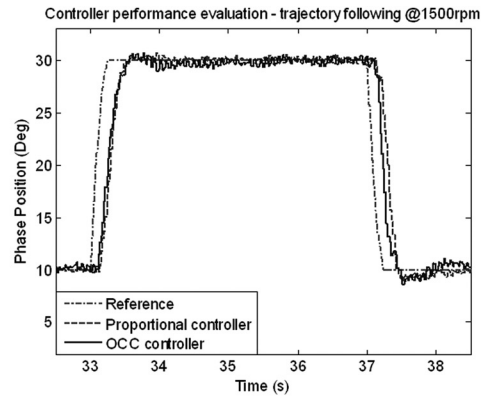
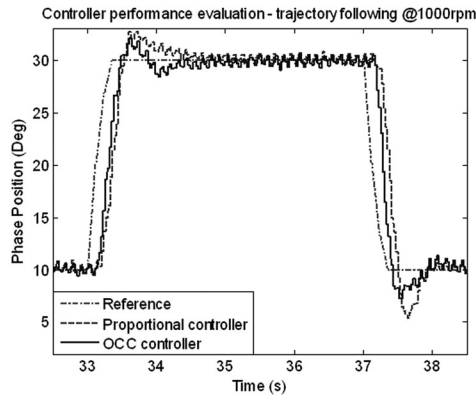


Fig. 12 EVVT phase tracking comparison

Controller design parameters were selected as

$$W_p = 1, \quad V = 0.01, \quad R = 1 \quad (58)$$

$$K_{OCC}(s) = \frac{60s^3 + 8.5 \times 10^2 s^2 + 1 \times 10^4 s + 6.7 \times 10^3}{s^4 + 148s^3 + 6937s^2 + 8.6 \times 10^4 s + 8.2 \times 10^4} \left(\frac{1000 \text{ rpm}}{\text{deg}} \right) \quad (59)$$

Using the OCC iterative control design algorithm in Ref. [18], an OCC controller was obtained

A proportional controller (60) was tuned for performance comparison. Note that the dc gains of both controllers are fairly close.

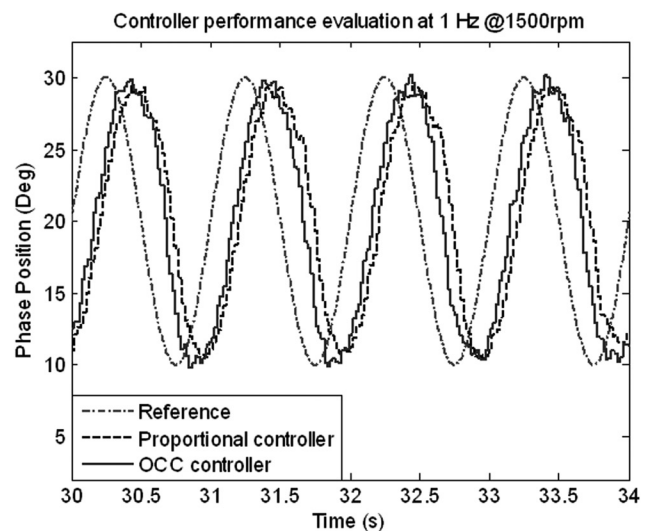
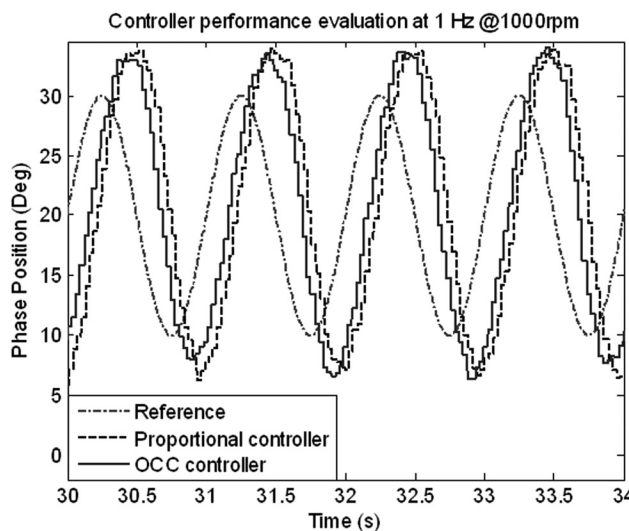
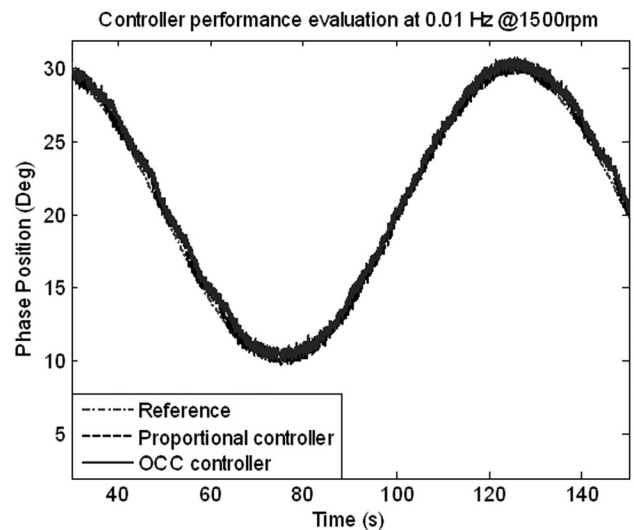
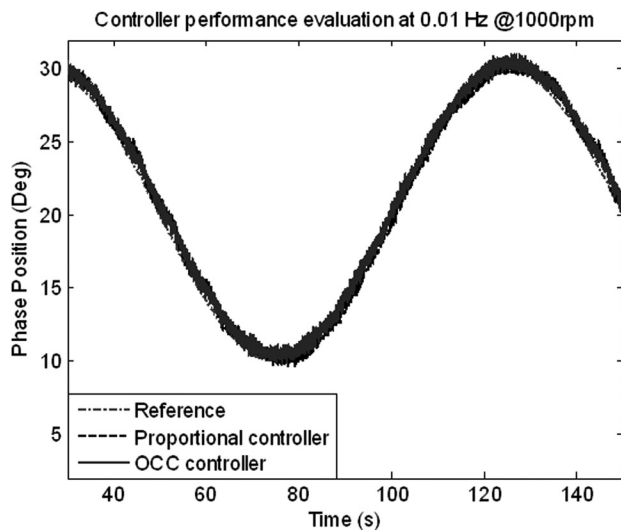


Fig. 13 Sinusoidal responses of the closed-loop EVVT system at 0.01 and 1.00 Hz

Table 6 Frequency responses of the closed-loop EVVT system

Input Frequency (Hz)	1000 rpm				1500 rpm			
	Magnitude		Phase (deg)		Magnitude		Phase (deg)	
	P	OCC	P	OCC	P	OCC	P	OCC
0.01	1	1	6	5	1	1	4	4
0.1	0.98	0.98	21	16	0.97	0.97	21	9
0.2	0.97	0.96	30	19	0.95	0.96	33	19
0.4	0.95	0.97	46	30	0.93	0.95	50	21
0.8	1.18	1.18	74	49	0.96	1.02	66	46
1	1.33	1.35	94	58	0.95	0.98	87	58
1.5	1.05	1.04	161	108	0.82	0.78	119	91
2	0.70	0.72	202	137	0.60	0.61	144	115

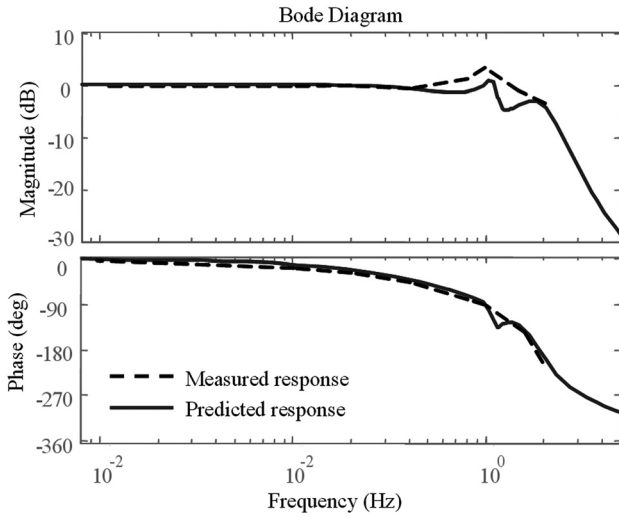


Fig. 14 Measured and identified EVVT frequency responses at 1000 rpm

The proportional controller was tuned to achieve fast response time with low overshoot at both 1000 and 1500 rpm for a square wave reference signal (see Fig. 11). Note that the same OCC controller was used at both engine speeds.

$$K_P(s) = 0.08 \text{ (1000 rpm/deg)} \quad (60)$$

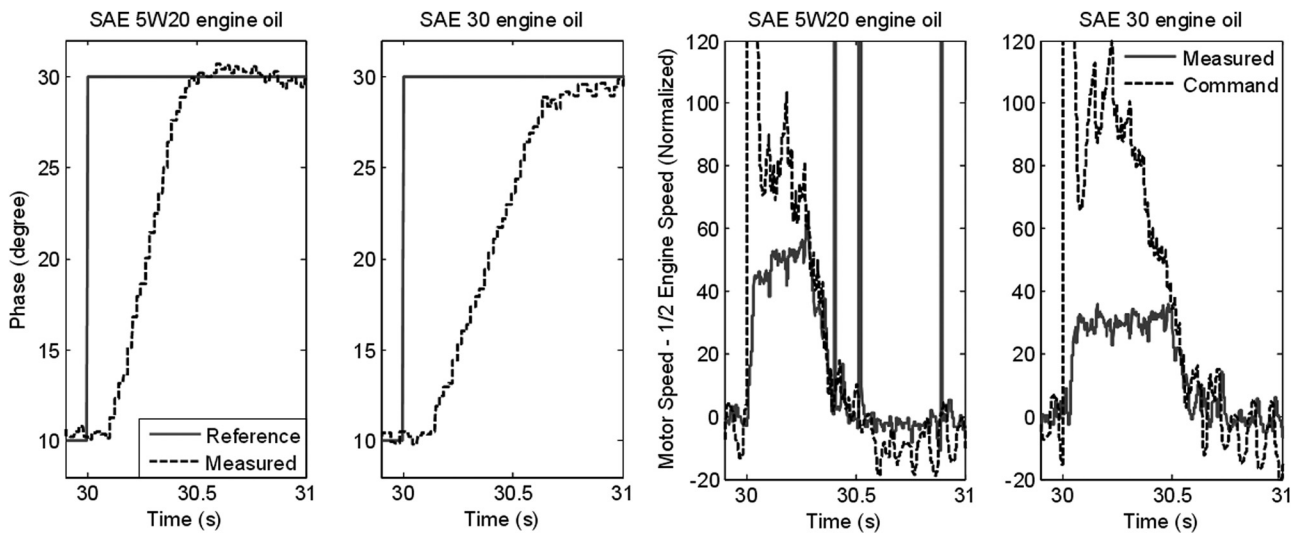


Fig. 15 Impact of engine oil viscosity on EVVT response

7.3 Control Performance Evaluation. The controllers were tested at 1000 and 1500 rpm. Both proportional and OCC controllers have feedforward portions from engine speed as shown in Eq. (38). Different reference signals were used to validate the trajectory tracking performance of the EVVT bench system.

The reference cam phase is a 20 crank degree phase advance or retard signal with a 10 deg linear phase change for the first engine cycle, 6.67 deg for the second, and 3.33 deg for the third, respectively. This signal was also used as the reference signal in simulations (Fig. 12). From Fig. 12, it is shown that the OCC controller has lower overshoot than the proportional controller at 1000 rpm. At 1500 rpm, overshoots for both controllers are very low. The OCC controller has a faster response time than the proportional controller in both engine speeds. Settling times for the two controllers are also very close to each other.

A series of sinusoidal waves was used to test the frequency response of the closed-loop systems to further investigate trajectory tracking performance of the EVVT controllers. The amplitude of the sinusoidal signal was set to be 10 deg and centered at 20 deg advance from the most retarded position, and the frequencies of the signals vary from 0.01 to 2.00 Hz. The test results show that both controllers have very good tracking performance at low frequency (see Fig. 13 and Table 6). As the excitation frequency increases, the phase responses associated with both controllers show increased phase lag with decreased magnitudes. The two controllers have almost identical gains at different frequencies, but the OCC has less phase delay than the proportional controller.

It was observed that when the test bench engine was running at 1000 rpm, the closed-loop EVVT system has overshoots when the excitation frequency is closed to 1.0 Hz. After 1.5 Hz, the system gain decays quickly. However, the frequency response of the identified fourth order nominal model in Eq. (56) does not show this behavior at 1.0 Hz. To study this phenomena, a seventh order model was obtained using closed-loop system identification at 1000 rpm and its frequency response (predicted performance) was compared with the measured data, obtained from magnitude and phase responses of the sinusoidal input at different frequency, in Fig. 14. A peak near 1.0 Hz can be found in the magnitude of the measured and predicted frequency responses. The overshoot of the closed-loop system can be duplicated under simulation environment using the identified seventh order model at 1000 rpm. However, the physical dynamics behind the phenomenon are still not clear and it is believed that it could be caused by the timing belt vibration.

7.4 Performance Variation Due to the Engine Oil Viscosity. Nonlinear friction in the hydraulic system [34] could also affect the performance of the EVVT. Two different types of

engine oil, SAE 5W20 and SAE 30, were used during the bench tests to study this effect. The engine was running at 1500rpm at room temperature (25 °C), and OCC controller (59) was used in both cases. The reference signal was a 20deg advance step. The 10–90% rising time was 0.3 s for SAE 5W20, and 0.48 s for SAE 30 engine oil. The response time difference is due to the viscous friction in the planetary gear system caused by the engine oil viscosity. Figure 15 shows the system step response and normalized speed difference between the EVVT motor and half engine speed (750 rpm). The EVVT motor speed was saturated at 30 units above 750 rpm with SAE 30 and at about 50 units above 750 rpm with SAE 5W20. The system response slows down as the difference between the EVVT motor and half of the engine speed increases. Notice that the EVVT motor speed is measured by calculating PWM frequency from the EVVT local speed controller.

The test result also suggests that the frictionless assumption during the simulation study is not true. However, on an actual engine, the nominal operating temperature is much higher than the room temperature and the engine oil viscosity will have much less effect for a warm engine than a cold engine.

As a summary, it was observed from the EVVT bench tests that the engine oil viscosity has a large impact on EVVT performance. Since the engine oil is used to lubricate the planetary gear system, the hydraulic friction introduced by the engine oil adds additional load to the electric motor and limits the peak motor speed. As a result the maximum phasing speed is reduced when high viscosity engine oil was used. Two kinds of engine oil with different viscosities were used on the test bench. The results show that at room temperature, the EVVT system response is 1.6 times slower using SAE 30 than using SAE 5W20 engine oil.

8 Conclusions

An EVVT system with planetary gear-train was modeled based upon individual system component kinematics and dynamics. A closed-loop OCC controller with feedforward was designed to reduce the cam phase tracking error during the SI and HCCI combustion mode transition, where the filtered derivative of the cam reference phase is used as the feedforward control. Compared to the well-tuned PD controllers, simulation results show that the OCC controller provides fast response with low overshoot and low tracking error.

An EVVT system was installed on an engine head and bench tests were conducted. The EVVT system plant model was obtained by using closed-loop system identification. The model has fairly similar responses to the physical system. An OCC controller was developed based on the identified model. Different signals were used as reference to test the controller performance. The experimental results showed that the OCC controller provides a faster response time than that of a well-tuned proportional controller. The OCC controller performance also has less phase delay than the proportional controller under high frequency sinusoidal reference input. The bench test results show that the OCC has a better overall performance and is suitable for an HCCI capable SI engine.

The impact of engine oil viscosity was also investigated. The test results showed that the EVVT response slows down as the engine oil viscosity increases. It suggested that it is necessary to use low viscosity engine oil to achieve the maximum performance. This could mean either operating at a high oil temperature or using low viscosity engine oil.

References

- [1] Moriya, Y., Watanabe, A., Uda, H., Kawamura, H., Yoshioka, M., and Adachi, M., 1996, "A Newly Developed Intelligent Variable Valve Timing System—Continuously Controlled Cam Phasing as Applied to New 3 Liter Inline 6 Engine," SAE Technical Paper No. 960579.
- [2] Dugdale, P. H., Rademacher, R. J., Price, B. R., Subhedar, J. W., and Duguay, R. L., 2005, "Ecotec 2.4L VVT: A Variant of GM's Global 4-Cylinder Engine," SAE Technical Paper No. 2005-01-1941.

- [3] Hattori, M., Inoue, T., Mashiki, Z., Takenaka, A., Urushihata, H., Morino, S., and Inohara, T., 2008, "Development of Variable Valve Timing System Controlled by Electric Motor," SAE Technical Paper No. 2008-01-1358.
- [4] Theobald, M., Lequesns, B., and Henry, R., 1994, "Control of Engine Load via Electromagnetic Valve Actuators," SAE Technical Paper No. 940816.
- [5] Sun, Z., and Kuo, T., 2010, "Transient Control of Electro-Hydraulic Fully Flexible Engine Valve Actuation System," *IEEE Trans. Control Syst. Technol.*, **18**(3), pp. 613–621.
- [6] Ma, J., Zhu, G., and Schock, H., 2010, "A Dynamic Model of an Electro-Pneumatic Valve Actuator for Internal Combustion Engines," *ASME J. Dyn. Syst., Meas. Control*, **132**(2), p. 021007.
- [7] Pierik, R. J., and Wilson, J. O., 1994, "Engine Timing Drive With Fixed and Variable Phasing," U.S. Patent No. 5,327,859.
- [8] Urushihata, H., and Lida, H., 2008, "Variable Valve Timing Control Device of Internal Combustion Engine," U.S. Patent No. 7,363,896.
- [9] Zhang, Y., Xie, H., Zhou, N., Chen, T., and Zhao, H., 2007, "Study of SI-HCCI-SI Transition on a Port Fuel Injection Engine Equipped With 4VVAS," SAE Technical Paper No. 2007-01-0199.
- [10] Cairns, A., and Blaxill, H., 2007, "The Effects of Two-Stage Cam Profile Switching and External EGR on SI-CAI Combustion Transitions," SAE Technical Paper No. 2007-01-0187.
- [11] Shaver, G. M., Caton, P. A., Edwards, C. F., Gerdes, J. C., and Roelle, M. J., 2005, "Dynamic Modeling of Residual-Affected Homogeneous Charge Compression Ignition Engines With Variable Valve Actuation," *ASME J. Dyn., Meas., Control*, **127**(5), pp. 374–381.
- [12] Shaver, G. M., 2005, "Physics Based Modeling and Control of Residual-Affected HCCI Engines Using Variable Valve Actuation," Ph.D. thesis, Stanford University, Palo Alto, CA.
- [13] Law, D., Kemp, D., Allen, J., Kirkpatrick, G., and Copland, T., 2001, "Controlled Combustion in an IC-Engine With a Fully Variable Valve Train," SAE Technical Paper No. 2001-01-0251.
- [14] Milovanovic, N., Chen, R., and Turner, J., 2004, "Influence of the Variable Valve Timing Strategy on the Control of a Homogeneous Charge Compression (HCCI) Engine," SAE Technical Paper No. 2004-01-1899.
- [15] Agrell, F., Angstrom, H., Eriksson, B., Wikander, J., and Linderyd, J., 2003, "Integrated Simulation and Engine Test of Closed Loop HCCI Control by Aid of Variable Valve Timings," SAE Technical Paper No. 2003-01-0748.
- [16] Zhu, G., and Skelton, R. E., 1994, "Integrated Modeling and Control for the Large Spacecraft Laboratory Experiment Facility," *J. Guid. Control Dyn.*, **17**(3), pp. 442–450.
- [17] Zhu, G., Grigoriadis, K. M., and Skelton, R. E., 1995, "Covariance Control Design for Hubble Space Telescope," *J. Guid. Control Dyn.*, **18**(2), pp. 230–236.
- [18] Zhu, G., Rotea, M. A., and Skelton, R., 1997, "A Convergent Algorithm for the Output Covariance Constraint Control Problem," *SIAM J. Control Optim.*, **35**(1), pp. 341–361.
- [19] Ren, Z., and Zhu, G., 2011, "Integrated System ID and Control Design for an IC Engine Variable Valve Timing System," *ASME J. Dyn. Syst., Meas., Control*, **133**(2), p. 021012.
- [20] Skelton, R. E., and Anderson, B. D. O., 1986, "Q-Markov Covariance Equivalent Realization," *Int. J. Control*, **44**(5), pp. 1477–1490.
- [21] Liu, K., and Skelton, R. E., 1991, "Identification and control of NASA's ACES structure," Proceedings of American Control Conference, Boston, MA.
- [22] Zhu, G., Skelton, R. E., and Li, P., 1995, "Q-Markov Cover Identification Using Pseudo-Random Binary Signals," *Int. J. Control*, **62**(1), pp. 1273–1290.
- [23] Zhu, G., 2000, "Weighted Multirate q-Markov Cover Identification Using PRBS—An Application to Engine Systems," *Math. Probl. Eng.*, **6**, pp. 201–224.
- [24] Shigley, J. E., and Mischke, C. R., 2001, *Mechanical Engineering Design*, 6th ed., McGraw-Hill, New York.
- [25] Phillips, C. L., and Harbor, R. D., 2000, *Feedback Control System*, 4th ed., Prentice-Hall, Englewood Cliffs, NJ.
- [26] Meerkov, S., and Runolfsson, T., 1989, "Output Residence Time Control," *IEEE Trans. Autom. Control*, **34**, pp. 1171–1176.
- [27] Wilson, D. A., 1989, "Convolution and Hankel Operator Norms for Linear Systems," *IEEE Trans. Autom. Control*, **34**, pp. 94–97.
- [28] Zhu, G., Corless, M., and Skelton, R., 1989, "Robustness Properties of Covariance Controllers," Proceedings of Allerton Conference, Monticello, IL.
- [29] Ren, Z., and Zhu, G., 2009, "Pseudo-Random Binary Sequence Closed-Loop System Identification Error With Integration Control," *Proc. Inst. Mech. Eng., Part I: J. Syst. Control Eng.*, **233**, pp. 877–884.
- [30] Codrons, B., Anderson, B. D. O., and Gevers, M., 2002, "Closed-Loop Identification With an Unstable or Nonminimum Phase Controller," *Automatica*, **38**, pp. 2127–2137.
- [31] Peterson, W. W., 1961, *Error Correcting Coding*, MIT Technical Press, Cambridge, MA.
- [32] Anderson, B. D. O., and Skelton, R. E., 1988, "The Generation of all q-Markov Covers," *IEEE Trans. Circuits Syst.*, **35**(4), pp. 375–384.
- [33] King, A. M., Desai, U. B., and Skelton, R. E., 1988, "A Generalized Approach to q-Markov Covariance Equivalent Realization for Discrete Systems," *Automatica*, **24**(4), pp. 507–515.
- [34] Shi, Y., and Burton, R., 2013, "Modeling and Robust Discrete-Time Sliding-Mode Control Design for a Fluid Power Electrohydraulic Actuator (EHA) System," *IEEE/ASME Trans. Mechatron.*, **18**(1), pp. 1–10.